Q. J. R. Meteorol. Soc. (2002), **128**, pp. 149–171

A simple conceptual model of cirrus horizontal inhomogeneity and cloud fraction

By S. A. SMITH[1,2]* and A. D. DEL GENIO[2]
[1]*Columbia University, USA*
[2]*NASA GISS, USA*

(Received 3 July 2000; revised 28 February 2001)

SUMMARY

A simple conceptual model of horizontal inhomogeneity and cloud amount in cirrus clouds has been formulated on the basis that internal horizontal inhomogeneity in the ice mixing ratio is due to variations in the cloud depth, which are assumed to be Gaussian. The use of such a model was justified by the observed relationship between the normalized variability of cloud depth and both the cloud amount and the normalized variability of the ice-water mixing ratio (and extinction).

Using radar cloud-depth data as input, the model reproduced well the in-cloud ice-water mixing ratio histograms obtained from horizontal aircraft runs during the FIRE-II cirrus campaign. For totally overcast cases the histograms were almost Gaussian, but changed as cloud amount decreased to distributions which peaked at the lowest non-zero ice value and decreased rapidly and monotonically towards higher ice values for cloud amounts below 90%. Cloud amounts and average ice-water mixing ratios for cases with observed distributions of cloud depth were predicted by the model to within 15% and 31% of the observed values. This model could be used as a starting point in the development of a GCM parametrization of the ice mixing-ratio probability distribution function and cloud amount, if a means of diagnosing the depth of the saturated layer and the standard deviation of cloud depth from basic large-scale meteorological parameters could be determined.

KEYWORDS: Cloud parametrization Ice histograms Ice sedimentation

1. INTRODUCTION

Cirrus clouds play a major role in the earth's radiation budget due to their extensive areal coverage. It is therefore important to improve their representation in general circulation models (GCMs) and to represent their subgrid-scale variability. The radiative properties of cirrus clouds depend not only on ice-water content (IWC) but also on the shape, orientation and size distribution of the ice crystals. However, GCMs do not predict these details, nor do they give the total ice-crystal concentration. So any parametrization must use the bulk properties of the cloud predicted by the GCM such as IWC, cloud height and cloud depth, or environmental parameters such as temperature or humidity, and diagnose other properties empirically or using simplifying assumptions (Del Genio *et al.* 1996; Donner *et al.* 1997).

Currently, GCMs use the plane parallel approximation to compute the horizontally averaged albedo. This uses only the mean value of the optical depth τ, and ignores the effect of horizontal inhomogeneity. This results in a positive bias in the average albedo. The only way they account for variability is through the use of a cloud fraction. For marine stratocumulus clouds, within-cloud variance is more important than, and increases with, cloud fraction (Cahalan *et al.* 1994). Liou and Rao (1996) showed that cloud horizontal inhomogeneity in cirrus clouds can play a significant, zenith-angle dependent role in determining the solar reflection and transmission patterns. Tsay *et al.* 1996) showed that cloud morphology affects the shape of the angular distribution of reflected radiance.

The independent pixel approximation (IPA) is one of the simplest methods of accounting for the effects of horizontal variability in τ on solar radiative transfer.

* Corresponding author: Met Office, Room 258, London Road, Bracknell, Berkshire RG12 2SZ, UK. e-mail: samantha.smith@metoffice.com

The IPA computes the average albedo for an array of elements with varying values of τ. Each element is treated as being plane parallel and net horizontal transport between elements is neglected. However, it is accurate for marine stratocumulus clouds as long as the liquid-water-content wave-number spectrum decreases as $k^{-5/3}$, where k is wave number, so that most variability is in the longer scales. The IPA requires knowledge of the probability distribution function (pdf) of τ, i.e. knowledge of higher moments as well as the mean. The approximation of the optical-depth distribution by idealized functions would make the IPA more efficient for use in GCMs.

Subgrid-scale variability also has implications for GCM parametrizations of microphysical processes. For example, many models now represent cirrus ice fallout using nonlinear relationships between crystal fall speed and IWC valid on the cloud scale (Heymsfield 1977). There is no a priori reason to believe that such a parametrization can be applied to an IWC averaged over hundreds of kilometres, since the atmospheric vertical velocities that oppose sedimentation are an order of magnitude or more weaker on the GCM grid scale (Donner *et al.* 1997). It is also important to be able to predict the cloud fraction in a GCM from the large-scale parameters using physically based parametrizations rather than the empirical or ad hoc schemes used in most current GCMs.

Wielicki and Parker (1994) retrieved the pdfs of liquid-water path (LWP) from Landsat images of boundary-layer clouds and found them to vary according to cloud fraction. Considine *et al.* (1997) developed a simple statistical model which reproduced this behaviour, assuming a Gaussian distribution of lifting condensation levels (LCLs). Donner *et al.* (1997) found that the histograms of the optical depth of large-scale cirrus in both the ISCCP* data and in their model results showed a peak at the lowest value of τ.

This paper investigates the ice-water content distributions observed *in situ* during the FIRE-II† cirrus campaign in November and December 1991. The distributions of ISCCP optical depths are also obtained for the same period and compared to the aircraft results. A simple extension of the Considine *et al.* model is presented which reproduces the observed pdfs and gives an estimate of cloud amount (i.e. cloud fraction), based on a Gaussian distribution of cloud depths and the assumption that internal inhomogeneity is due to this variability in cloud depth.

Section 2 describes our data sources and processing techniques. Section 3 presents the resulting statistics of the observed cirrus, while section 4 describes the conceptual model motivated by these observations. The model is applied to each FIRE-II flight in section 5, and the ramifications of the model for the eventual parametrization of cirrus subgrid variability in GCMs is discussed in section 6.

2. Measurements

In situ measurements through cirrus clouds were taken by the National Center for Atmospheric Research (NCAR) Kingair (KA) and Sabreliner (SA) aircraft. The aircraft made several straight horizontal runs through the cirrus cloud, identified in this paper by the sortie number, e.g. KA03. The instrumentation on board the aircraft is described by several NCAR bulletins, but a brief description will be given here.

The Rosemount thermometer gives temperature data with an accuracy of ± 1 degC and resolution 0.006 degC. Although this probe may suffer from wetting effects in warm clouds, the problem is negligible in cirrus (Heymsfield *et al.* 1990). Relative changes are fairly reliable providing that the aircraft is not changing altitude.

* International Satellite Cloud Climatology Project.
† First ISCCP Regional Experiment II.

Humidities are obtained from the cryogenic hygrometer (a chilled mirror device), which has a fast time response due to the use of liquid nitrogen as a heat sink. The relative humidities, RH, were corrected for a 10% overestimation observed by Heymsfield and Milosevich (1995) for these FIRE flights, which appeared to be independent of temperature or the presence of liquid water. The hygrometer also has a tendency to overshoot when the RH changes rapidly, but average values should be reliable. The EG+G hygrometer is not used because it responds slowly and its accuracy is dubious at the low temperatures associated with cirrus clouds.

Cloud microphysical data were obtained during horizontal runs within cloud using the Particle Measuring Systems 2D-C and 2D-P optical array probes (Knollenberg 1970; Heymsfield and Baumgardner 1985) averaged over 5 s intervals. This corresponds to a maximum spacing of 600 m for the Kingair data and 1 km for the Sabreliner data (maximum air speeds for the Kingair and Saberliner of 120 m s^{-1} and 200 m s^{-1}, respectively). The ice-crystal size spectra from the 2D-C and 2D-P probes are merged so that data for crystals smaller than 400 μm are given by the 2D-C probe, and data for larger crystals are given by the 2D-P probe. Then the IWC is calculated from the ice-crystal size spectra using empirical equations for the mass of each ice crystal as in Heymsfield (1977), giving values correct to within a factor of 2 (Heymsfield *et al.* 1990). Uncertainties in IWC are due to the use of these empirical relationships between the mass and size of the crystals and due to particles which are too small to be detected. Histograms of these IWCs were obtained for each flight. The consistent behaviour of the histograms relative to the cloud amount, and of the IWC variance relative to independent measures of cloud depth, argues directly for an IWC error bar considerably smaller than the formal estimate for most measurements. Ice-crystal effective radii r_e were calculated using the definition of Foot (1988), which preserves the measured IWC and cross-sectional area and is valid regardless of crystal shape. The visible extinction was computed as the geometric optics limit of $2 \times A_T$, where A_T is the total crystal cross-sectional area, as in Fu (1996).

The Penn State University (PSU) 94 GHz (or 3 mm) radar collects vertical profiles of reflectivities. It therefore provided an estimate of the depth D of the cirrus that drifted over the main operations centre in Coffeyville. The radar data gives very accurate estimates of cloud-base height and is very sensitive to large cloud particles. Its longer wavelength means it cannot detect the very small particles detectable by the lidar. Likewise, the aircraft has problems seeing the very smallest particles. The lidar signal, on the other hand, is attenuated by an ensemble of larger particles. Despite these differences, cloud variability appears to be well represented by each instrument. Uttal *et al.* (1995) found that the Environmental Technology Laboratory (ETL) radar, the PSU radar and the ETL lidar all observed similar distributions of cloud heights. The minimum detectable signal for this data was in the -25 to -30 dbZ range, and so the radar will miss on average the top 20–30% of the layers, although this depends on the cloud layer being observed (Mace *et al.* 1997). The cloud depths estimated from the radar data were used in those cases where the flight took place over and around Coffeyville itself (usually within 40 km of Coffeyville but occasionally extending further away). There were some flights which took place in other areas. In these cases, when the entire flight was more than 100 km away from Coffeyville, the radar data was unrepresentative of the area sampled by the aircraft, and therefore the cirrus cloud depth was estimated from the aircraft profiles combined with the humidity profile obtained from the CLASS* sonde launched closest to the aircraft flight path (usually within 40 km). The radar data were

* Cross-chain Loran Atmospheric Sounding System.

averaged every 10 s, corresponding to 300 m spacing for a wind speed of 30 m s^{-1}, which is comparable to the ice data.

Optical depths were retrieved from the ISCCP pixel-level data. Individual pixel-level ISCCP data consist of values retrieved from radiances measured by pixels of 5 km size and spaced 30 km apart. These represent a sample of the distribution of cloud conditions over this larger sampling spatial scale, and are recorded every 3 hours. A comprehensive description of the data is found in Rossow and Schiffer (1991). The visible optical depth is retrieved from observed visible radiances using a model of an ice cloud composed of fractal poly-crystals with a cross-section-weighted radius of 30 μm, and can be used to calculate the amount of solar radiation reflected by clouds.

3. Cloud-depth distributions

Figure 1 shows the cloud-depth distributions observed by the radar. The curves through these are Gaussian distributions of cloud depth having the observed mean cloud depth $\overline{D}$ and its standard deviation σ_D. Some of the histograms fit the Gaussian distribution better than others. The cirrus thickened and its base descended very rapidly (cloud depth doubled within half an hour) during flight SA08, and the cirrus descended and merged with an underlying nimbostratus layer during KA10. These non-stationary cases did not have Gaussian distributions of cloud depth and therefore were not included in the analysis. The cloud boundary statistics for the remaining cases are given in Table 1.

The cloud-depth distributions can be approximated using a Gaussian distribution either by taking the whole flight period or by splitting it up into parts. Those histograms which are bimodal are due to the variation in average cloud thickness with time. Such variations can be due to changes in the synoptic forcing or due to internal evolution of the cirrus itself, as a result of the onset of convective generation or sedimentation. This introduces ambiguity into our analysis, because aircraft runs do not always sample all phases of the life cycle. Since the time-scale of these variations is comparable to or longer than a GCM physics time step, we divide such cases into two segments with unimodal behaviour when necessary and include the segment which corresponds to the aircraft data. Figure 2 shows these distributions while Fig. 3 shows examples of

TABLE 1. Aircraft and radar observations

Flight	CA (%)	Radar	D_G (m)	$\overline{D}$ (m)	σ_D (m)	A_0 (10^{-7} m^{-1})	$\overline{w_i}$ (10^{-5})
KA04	100	Y	1400	4750	311	3.0	7.0
KA07	100	Y	1400	2466	357	1.5	9.2
KA14	90	Y	1000	3230	285	2.5	4.9
KA13	81	Y	400	922	270	1.5	2.3
KA02	73	Y	500	1084	311	2.0	5.3
KA07NW	100	N	1500	2500	285	1.5	9.2
SA07	100	N	1500	2000	300	1.0	12.0
SA05	70	N	500	700	358	1.0	6.7
SA06	70	N	500	2200	600	1.0	2.9
SA09	70	N	1000	1700	600	1.0	11.3
SA14	58	N	400	1700	800	1.0	7.6
SA13	51	N	300	1600	800	0.5	1.4
KA05	97	N	1000	1700	235	1.3	1.8

Observations of cloud amount CA, generating-layer depth D_G, average cloud depth $\overline{D}$ and its standard deviation σ_D, adiabatic ice-water content gradient A_0 representative of the generating layer, and the cloud average ice-water mixing ratio $\overline{w_i}$. The third column indicates whether radar data were available (Y) or not (N).

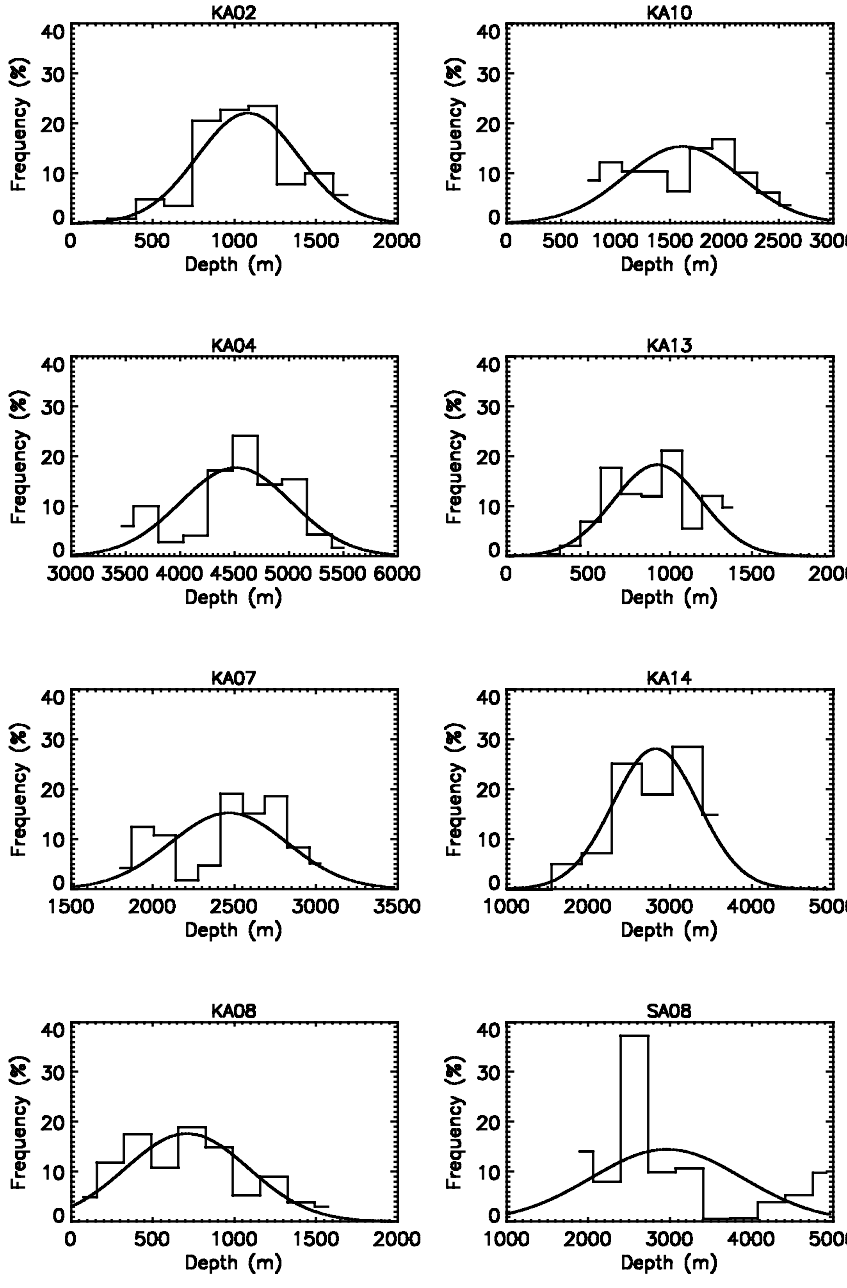

Figure 1. Histograms of cloud depth as measured by the PSU 94 GHz radar during eight aircraft sorties. The curves are Gaussian distributions having the observed mean $\overline{D}$ and standard deviation σ_D of cloud depth.

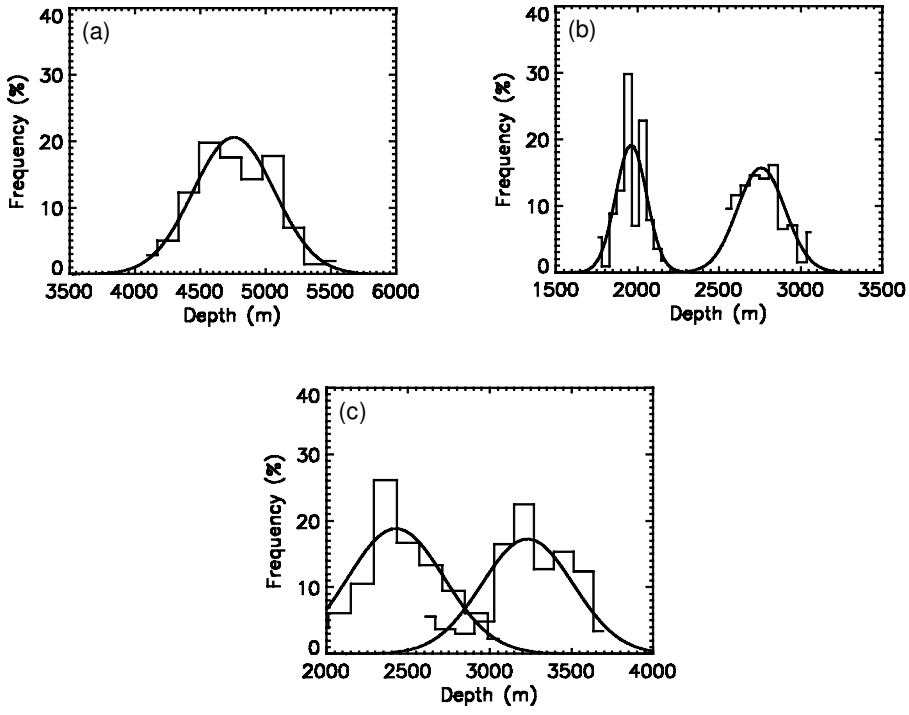

Figure 2. Histograms of cloud depth as measured by the radar for flights (a) KA04, (b) KA07 and (c) KA14, split into time periods during which the average depth remained approximately constant. The curves are Gaussian distributions having the observed mean $\overline{D}$ and standard deviation σ_D of cloud depth for each time period.

the cirrus cloud boundaries for these cases. The short dashed lines show the times and altitudes of the aircraft runs which took place during these times over Coffeyville.

The cirrus layer observed during flight KA04 became thinner in time, unless the crystals at cloud top where too small to be detected. However, the fact that radar-observed cloud base descended indicates that there was a real variation in the average layer characteristics. Most of the aircraft runs took place between the times of 0100 and 0217 UTC, before the base descended, and therefore only radar data from this part of the flight period was used to obtain $\overline{D}$ and σ_D. The cirrus observed during KA07 seemed to become thinner in the second half of the flight before deepening again. The cloud-depth time series can be split into two halves—part A (flight start time to 2020 UTC) and part B (between 2023 and 2042 UTC), each of which approximates to a Gaussian distribution. However, the variation in cloud depth was due to variation in radar cloud-top height, which can be unreliable in the presence of smaller particles, and it increased again later, indicating that any variation, whether in cloud depth or particle size, is part of the horizontal inhomogeneity which we are trying to reproduce. The aircraft runs took place during both halves, and therefore the cloud-depth statistics for the entire flight period were used. Also, the cirrus observed during KA14 was thinner during the second half, when most of the runs took place. This was also split into two parts—part A (between 1440 and 1527 UTC) and part B (between 1530 and 1612 UTC), producing two overlapping Gaussian distributions. The change in time is mainly due to the lowering of radar cloud-top height, until the very end when the cloud starts to dissipate. The last aircraft run observed cloud above the radar-observed cloud-top height. Therefore, the

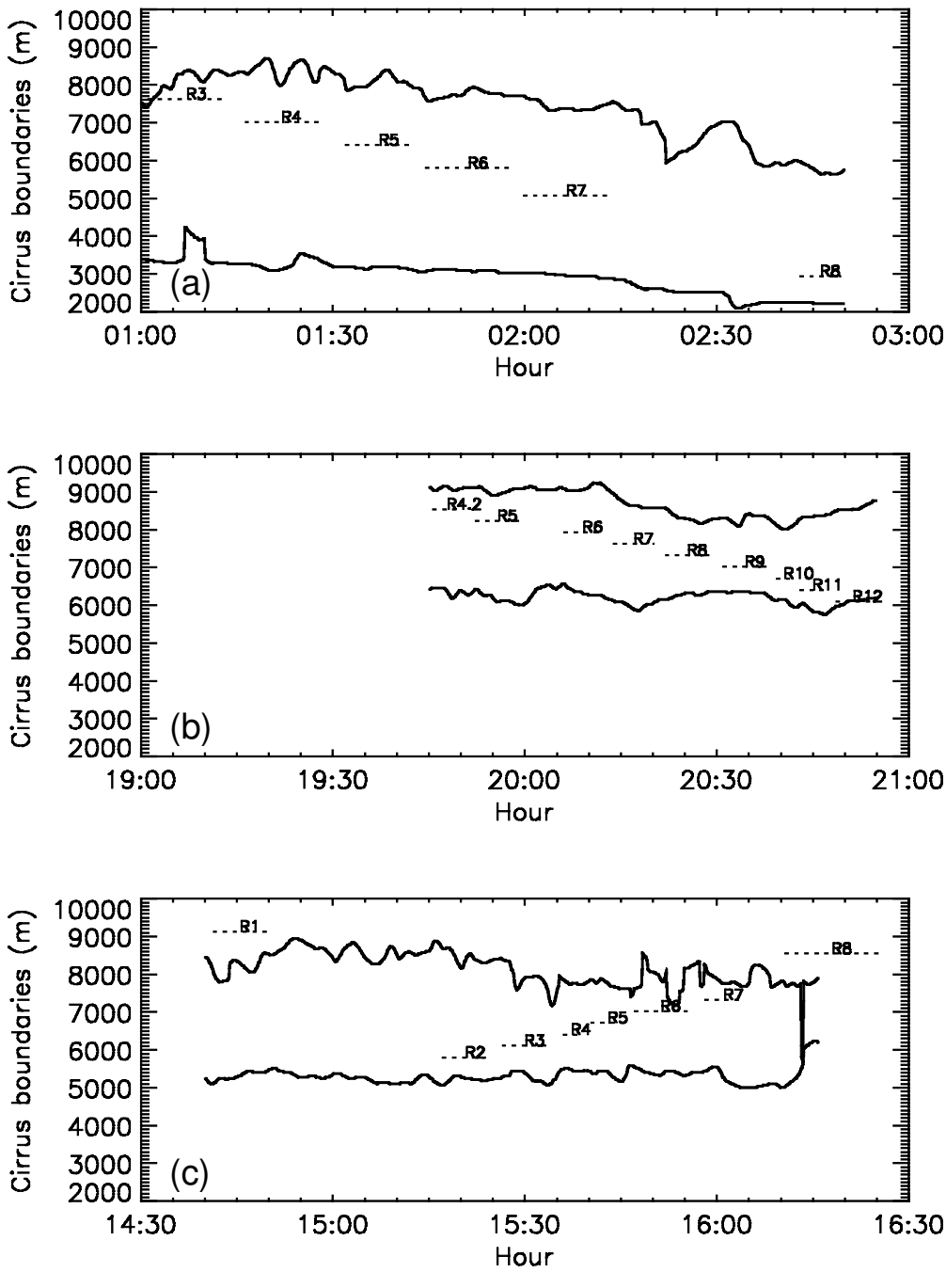

Figure 3. Cirrus cloud boundaries as measured by the radar for flights (a) KA04, (b) KA07 and (c) KA14. The short dashed lines show the times (UTC) and altitudes of the aircraft runs which took place during these times over Coffeyville.

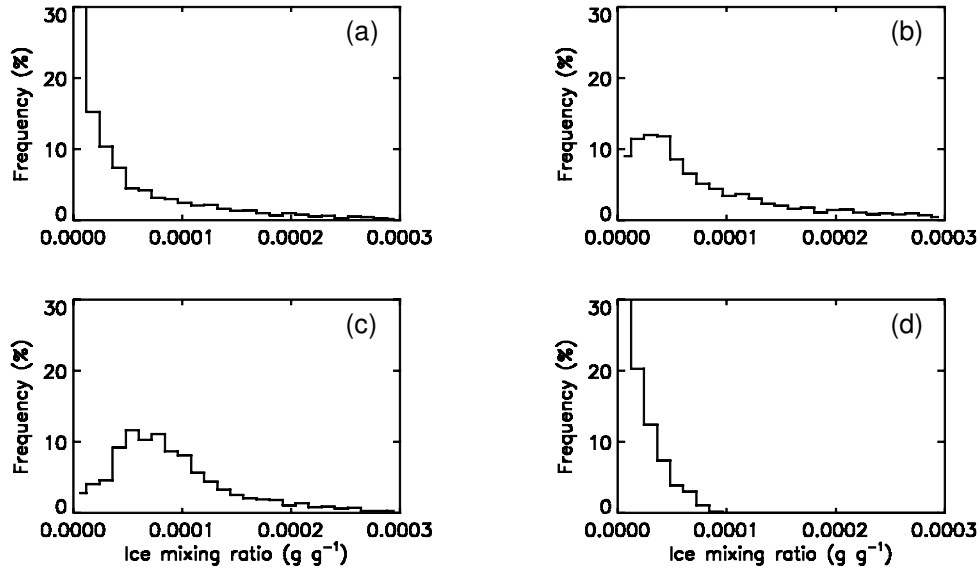

Figure 4. Composite histograms of ice-water mixing ratio (g g^{-1}) for the various regimes of cloud amount CA: (a) CA $\leq$ 89%, (b) 90% $\leq$ CA $\leq$ 99%, (c) CA = 100%, and (d) Flight KA05.

average cloud depth from part A was used, and the standard deviations from the two parts were averaged together.

4. Observed histograms

Figure 4 shows the composite histograms of ice-water mixing ratio (g g^{-1}) for various cloud amount regimes. Cloud amount CA was determined as the percentage of all runs during which the aircraft was within cirrus cloud. The ice mixing-ratio histograms for totally overcast cases (CA = 100%) only deviate slightly from Gaussian (only slightly skewed). As cloud fraction starts to decrease the mode shifts to smaller values and the histogram becomes more skewed. For cloud fractions below 90%, the histogram peaks at the smallest measurable value and decreases monotonically.

The ISCCP optical-depth histograms exhibit the same change in shape with changing cloud amount as shown in Fig. 5, although the distributions tend to be a little narrower because the sparse sampling of ISCCP reduces the probability of observing extreme values. An enlarged region of cirrus was chosen that included the smaller region sampled continuously by the aircraft during each flight, so that enough cloudy pixels were used to obtain reasonable statistics (at least 100, more if possible). Cloud amount was determined as the number of pixels used which actually contained cirrus cloud. These are smaller than the aircraft cloud amounts because rectangular regions which included some clear regions around the edges were used, though an attempt was made to minimize this. The basic similarity between the histograms in Figs. 5 and 4 suggests that the IWC and ice-water path (IWP) distributions are related, and that a model that captures the essential features of small-scale IWC or IWP variability will be useful in calculating the mean radiative impact of an inhomogeneous cirrus cloud.

The ice mixing-ratio histogram for the cirrus observed during flight KA05 peaked at the minimum possible ice mixing-ratio value, despite the fact that CA was high (97%). This cirrus had a very low average IWC (see Table 1) and very large crystals. It

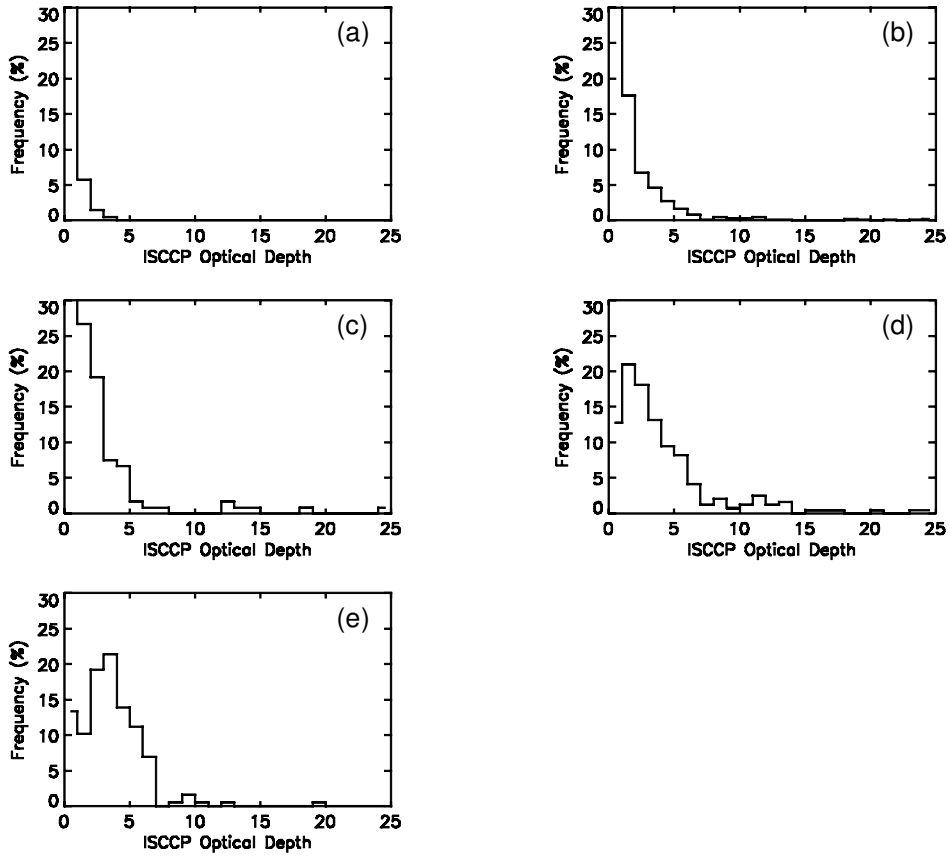

Figure 5. Composite ISCCP optical-depth histograms for various regimes of cloud amount CA: (a) Cirrus bands, (b) CA < 60%, (c) CA < 63%, (d) CA < 71%, and (e) CA < 81%.

was optically very thin and had little turbulence, with wave-like vertical-velocity time series for all in-cloud runs. The IWC power spectrum decreased as $k^{-5/3}$, indicating transport by quasi-two-dimensional horizontal eddies and no convection, and the ratio of the turbulent kinetic-energy dissipation rate in the vertical to that in the horizontal was always smaller than 0.3. There was a very high vertical shear in horizontal wind speed across the entire cloud layer, and the atmosphere was very stable between 4 and 9 km.

5. CIRRUS CONCEPTUAL MODEL BASED ON CLOUD-DEPTH VARIABILITY

The shape of the distributions of both the *in situ* IWC and the ISCCP optical depths vary with cloud amount in a way which is similar to that observed for LWP of marine stratocumulus clouds (Wielicki and Parker 1994). Taking the average IWC and the standard deviation (σ_{IWC}) from all horizontal runs for each cloud, it has been shown in Smith and Del Genio (2001) that σ_{IWC} is proportional to the average IWC. A similar relationship was found for marine stratocumulus cloud LWP (Considine *et al.* 1997). The similarities between the two cloud types is quite surprising considering the different formation and maintenance processes, and it suggests the possibility of modelling cirrus horizontal inhomogeneity using a model similar to that used by Considine *et al.* (1997),

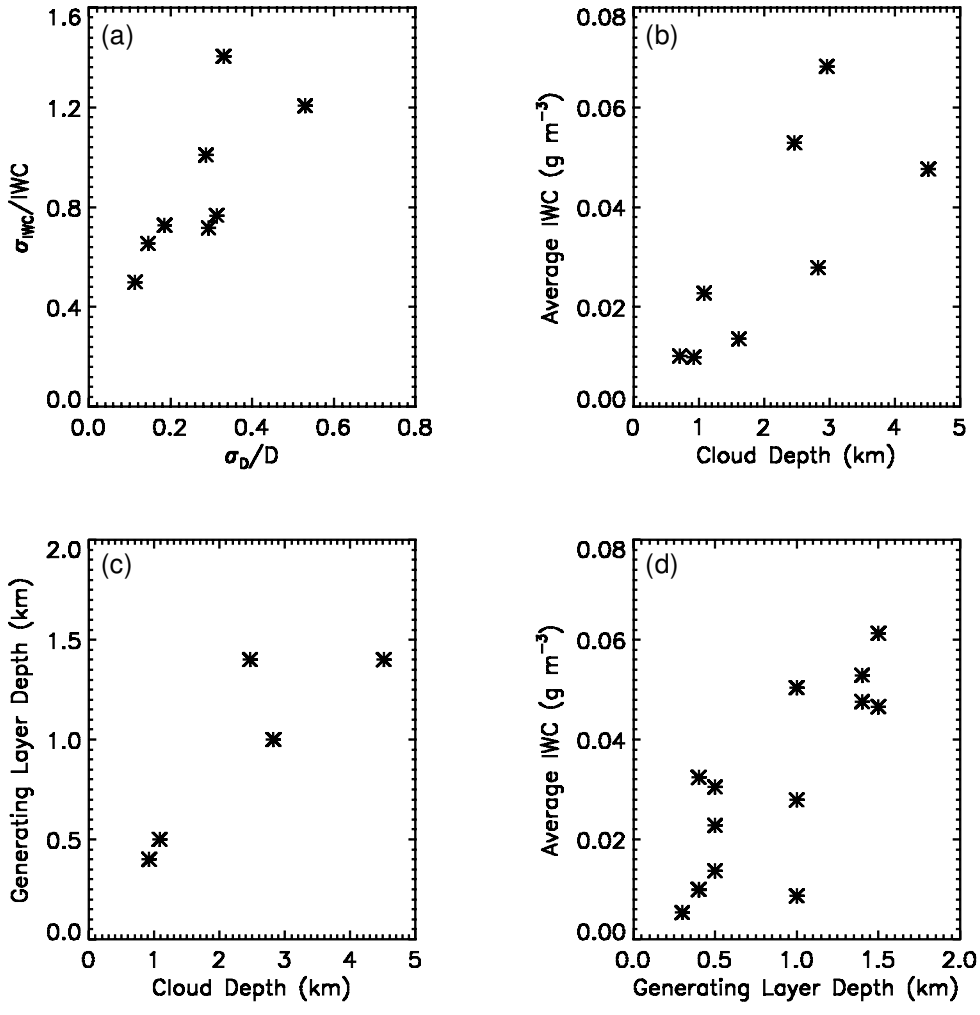

Figure 6. (a) Normalized variations of ice-water content IWC against normalized variations of cloud depth D, for those flights with radar data available. (b) Flight IWC against average cloud depth, for those flights with radar data available. (c) Generating-layer depth D_G against D, for those flights with both radar and good relative humidity data available. (d) Flight average IWC against average D_G, for those flights with good relative humidity data available.

whose basic assumption was that the internal cloud variability was due to air parcels having widely varying LCLs which were Gaussian in their distribution about the mean.

To further justify the use of an ice variability and cloud-amount parametrization based on variability in D, the relationship between these was investigated. Figure 6 shows the relationships between D, the generating-layer depth D_G (defined later) and IWC. There is a positive correlation between the normalized variations of IWC and those of D, suggesting that to zeroth order the microphysical variability can be attributed to the variation in D (or vice versa). Also, the average IWC is positively correlated with both D and D_G. Although not shown, the variability in radiative properties of the clouds, represented by visible extinction β, is also correlated with the variability in D. The generating-layer depth appears to be correlated with cloud depth, although there are not

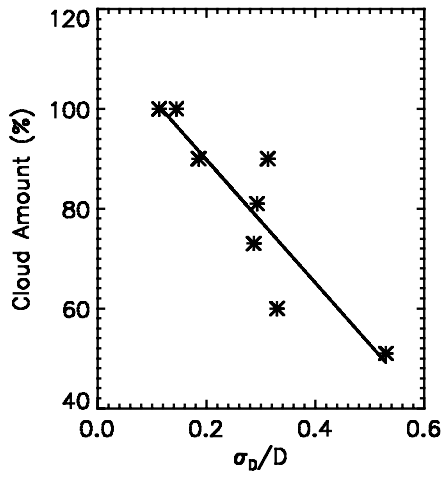

Figure 7. Observed cloud amount against the normalized variations of cloud-depth D observed by the radar.

enough data points to confirm this (few flights had both radar and RH data). Figure 7 shows that for radar observations, the cloud amount decreases for larger normalized cloud-depth variabilities, indicating that a model using cloud-depth variability could be used to obtain the cloud fraction.

Of course, IWC can vary locally for many reasons such as horizontal advection, entrainment and inhomogeneity of convective generation, and this may partly account for the scatter seen in Fig. 6. However, as long as other sources of variability are similarly distributed and uncorrelated with the variability in depth, a simple conceptual model based on the statistics of D should capture the essential features of IWC inhomogeneity. Note that it is the vertically integrated IWP rather than the local IWC that is relevant to the radiative effect of the cloud. We will relate the two very simply in the following section.

The mechanisms for the formation and growth of cirrus clouds are different from those for stratocumulus clouds. Ice initially forms in ascending air which becomes saturated with respect to water. Eventually the growing ice crystals will use up all the available vapour, reducing the humidity to ice saturation, especially if there are many crystals and ascent velocities are low. The amount of ice initially increases by deposition of vapour, but eventually ice settling becomes equally important as the crystals become large.

In a fully developed cirrus cloud, deposition balances fallout (Heymsfield and Donner 1990). Thicker clouds have usually grown down from an original generating layer near cloud top due to evaporation of falling ice which moistens the underlying layers. To demonstrate this, the average IWC and RH from each horizontal run for the three thickest cirrus clouds observed are shown in Figs. 8 and 9, together with the standard deviations. Throughout the paper RH is with respect to ice saturation, the relevant state once a cirrus cloud has proceeded beyond the initial nucleation phase. The upper and lower boundaries of the supersaturated region are assumed to define D_G. These cirrus have a layered structure in the vertical, with supersaturated upper regions and subsaturated lower regions. They all have thin stable layers at cloud base and at the base of the saturated region. The cirrus cloud from flight KA04 had a very obvious cloud-top generating layer, while the one from KA07 had two generating layers in the

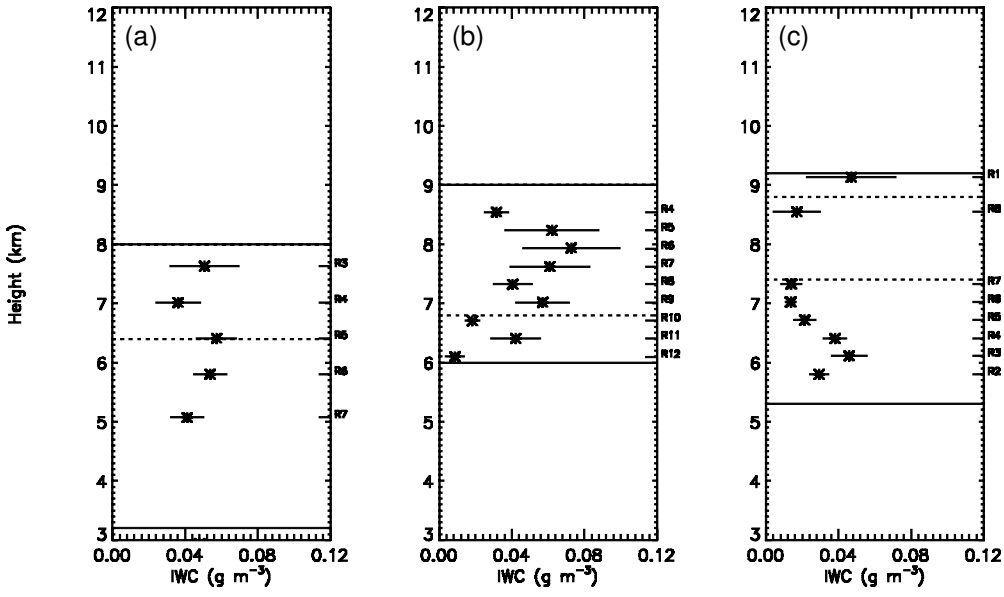

Figure 8. Average ice-water content profiles for (a) flight KA04, (b) flight KA07, and (c) flight KA14. The standard deviations are shown as horizontal lines through the symbols. The solid lines depict cloud base and cloud top, while the dashed line shows where the ice-saturated region lies.

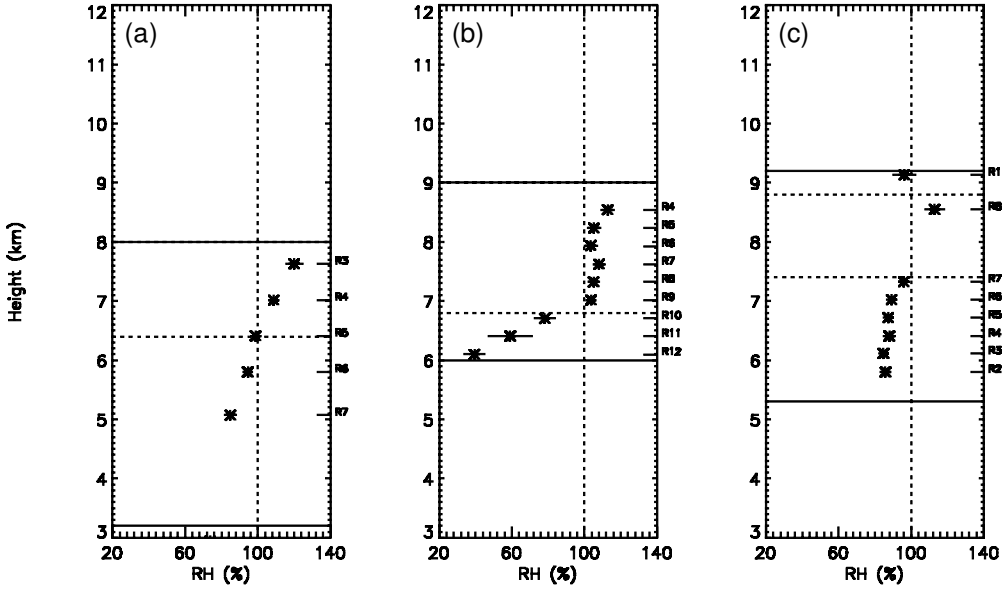

Figure 9. As in figure 8 but for average relative humidity with respect to ice.

saturated region, as seen in the layered structure of both the IWC and the RH. The cirrus observed during KA14 had started to dissipate and therefore gravitational settling was dominating over ice nucleation, ice was falling out of the saturated layer into the layers below, and crystals were accumulating near cloud base with a maximum IWC there. The very top region is subsaturated owing to this descent, and was probably part of the original generating layer.

The very different IWC profiles illustrated in Fig. 8, capturing different clouds in different stages of their evolution, can only be understood with a detailed cirrus cloud model. Fortunately, vertical redistribution of ice has no impact on the vertically integrated IWP and we need only predict the shape of the IWC distribution, not the local values of IWC, for potential applications to GCMs. In the following paragraphs we describe a simple extension of the Considine *et al.* (97) conceptual model that fits the FIRE-II cirrus data and may therefore serve as a starting point for the development of a GCM parametrization of subgrid-scale variability.

Consider the initial formation of the cirrus cloud when ice crystals are still small. The total-water mass mixing ratio is conserved ($w_t = w_v + w_i$, where w_v is the vapour mixing ratio, defined as the ratio of the mass of water vapour to the mass of dry air, and w_i is the ice mass mixing ratio). During this initial part of the cloud life cycle, we can assume adiabatic motion, and the ice-water mixing ratio of an air parcel will be equal to the excess water vapour due to the decrease in the saturation vapour mixing ratio w_{sat} with height:

$$w_i = w_t - w_{sat}. \tag{1}$$

So the vertical gradient in IWC, A_0 (m^{-1}), is given by differentiating this with respect to height z. Assume air pressure p is constant (thin layer), and $d/dz = (dT/dz)\, d/dT$, where T is temperature.

$$A_0 = \frac{dw_i}{dz} = \frac{dw_{sat}}{dz} = \frac{\varepsilon}{p}\frac{de_{sat}}{dz} = \frac{\varepsilon}{p}\frac{dT}{dz}\frac{de_{sat}}{dT} = \frac{\varepsilon}{p}\frac{dT}{dz}\frac{L_s e_{sat}}{R_v T^2} = \frac{w_{sat} L_s \Gamma_m}{R_v T^2}, \tag{2}$$

where the moist adiabatic lapse rate Γ_m is given by

$$\Gamma_m = \frac{\Gamma_d\{1 + (L_s w_{sat})/(R_d T)\}}{1 + (w_{sat}\varepsilon L_s^2)/(c_p R_d T^2)}. \tag{3}$$

In (2) and (3) e_{sat} is the saturation vapour pressure, L_s is the latent heat of sublimation (2.84×10^6 J kg^{-1}) and c_p is the specific heat capacity at constant pressure (1005 J $K^{-1}kg^{-1}$); R_v and R_d are the gas constants for vapour (461.5 J $kg^{-1}K^{-1}$) and dry air (287 J $kg^{-1}K^{-1}$), respectively, with ε being their ratio (0.622). The difference between Γ_m and Γ_d decreases with decreasing T, and so A_0 decreases with height over the full depth of the cloud. However, the variation is not substantial over typical generating-layer depths of between 300 m and 1.5 km near cloud top (or alternatively, over the depth of a GCM layer, which is comparable).

Therefore, at any level z above the local base of the cirrus generating layer, the ice-water mixing ratio can be approximated by the first term in the Taylor-series expansion as $w_i \sim A_0 z$. The IWP is the adiabatic ice-water mixing ratio integrated over the depth of the generating layer, and so

$$\mathrm{IWP} = \frac{A_0 D_G^2}{2}. \tag{4}$$

This expression applies strictly only to the initial generating stage, when D_G and actual cloud thickness are equal. In the mature stage of development, sedimentation extends cloud base downwards so that D is greater than D_G and w_i is no longer a monotonically increasing function of z (Fig. 8; see also Heymsfield and Donner 1990). However, as long as sublimation of falling ice has not yet dissipated a significant fraction of the cloud, the expression above still gives a valid estimate of IWP, since sedimentation only redistributes ice in the vertical.

If there is a one-to-one correlation between D_G and IWP (for positive D_G), we can relate the pdfs by

$$P(\mathrm{IWP})\,\mathrm{d}(\mathrm{IWP}) = P(D_G)\,\mathrm{d}(D_G).$$

We do not know if this is the case, since IWP itself is not observed and only one estimate of D_G exists per aircraft flight. The conceptual model above, which is based on the observed similarity of IWC and D statistics (Fig. 6), suggests that this is a reasonable working hypothesis. We therefore assume that

$$\frac{P(D_G)}{P(\mathrm{IWP})} = \frac{\mathrm{d}(\mathrm{IWP})}{\mathrm{d}D_G} = A_0 D_G. \tag{5}$$

If we further assume that the standard deviation of D_G (which we cannot observe) is similar to the observed σ_D, the pdf of the IWP is given by (following Considine *et al.* 1997)

$$P(\mathrm{IWP}) = \frac{1}{\sqrt{2A_0\mathrm{IWP}}} \frac{1}{\sqrt{2\pi\sigma_D^2}} \exp\left\{ \frac{-(\sqrt{2\mathrm{IWP}/A_0} - \overline{D_G})^2}{2\sigma_D^2} \right\}. \tag{6}$$

This is the fundamental relationship for assessing cirrus radiative properties. However, the aircraft measures the ice mixing ratios at various levels within the cirrus clouds, so we must convert IWP in (6) to IWC for comparison to the observations.

As mentioned above, the observed clouds have matured past the initial formation stage to a stage where there has been a downward redistribution of the ice mass by gravitational settling. This affects the mean IWC at each altitude, and it also shifts the IWC statistics from the Gaussian shape implied by the linear behaviour of adiabatic IWC to the skewed distributions observed (Fig. 4), because larger IWC points will lose more mass through fallout than small IWC points, shifting the distribution away from large IWC values and towards small IWC values, while a very few large IWC values from the base of the cloud extend the large IWC tail. The effect on the magnitude of the horizontal variability should not be large, however, relative to other uncertainties. Thus, we expect the IWC and IWP pdfs to have similar shapes, and this is qualitatively borne out by the similarities we observe in the aircraft IWC pdfs (Fig. 4) and those of optical thickness (Fig. 5).

The observed IWC profiles (Fig. 8) do not conform to any single shape, which changes with the development of a cloud. This is further complicated by the vertical sampling of the cloud being different for each case. So it is assumed that IWC is independent of height for simplicity, and that the aircraft-measured average ice-water mixing ratio $\overline{w_i}$ is representative of the average value at all levels in the cloud. Ice-water mixing ratio is therefore obtained by dividing the modelled IWP by average D for comparison with the aircraft data, while the distribution $P(w_i)$ will have the same shape as $P(\mathrm{IWP})$ as described above and supported by the similarity in Figs. 4 and 5. This accounts for the effect of ice sedimentation on the observed ice-water mixing ratios by spreading the ice through a region deeper than D_G. In other words, the model estimates

IWP as the adiabatic IWC integrated over D_G; to relate this to the data, actual (sub-adiabatic) IWC values must be integrated over the full cloud depth.

The cloud amount is predicted from the modelled distribution as the percentage of the distribution with IWP above a threshold value of 2×10^{-7} g g^{-1}, equivalent to a D_G of about 10 m. The average ice mixing ratio is found by integrating $w_i P(w_i)$ for all values of w_i greater than the threshold.

We note that our model for cirrus is based on the variability statistics of cloud depth, whether these arise from variations in cloud base, cloud top, or both (Figs. 1, 2 and 3). Considine *et al.*'s model for marine stratocumulus ascribed all variability to cloud base under a uniform inversion. This distinction is less important than the more general statement about Gaussian-distributed cloud boundaries apparently common to both cloud types.

6. Results

The model was run for all of the stationary FIRE-II cirrus flights during which the cryogenic hygrometer was working, as accurate RH measurements are required for estimating the depth of the cirrus-generating region in each case. Generating-layer depths were estimated as the depth of the cloud over which the air was supersaturated with respect to ice, using the corrected cryogenic hygrometer RHs from the horizontal runs and from the profiles at the start and end of each flight. Aircraft sampling introduces uncertainties into these estimates for certain flights. For example, if only two runs were saturated, the distance between them was used as the generator depth unless the profile suggested a deeper layer. Some cases appeared to have a steady gradient in RH, and then the height at which 100% RH was reached could be estimated. When there appeared to be more than one generating layer, D_G was given a value equal to the total depth of the layers. Values of A_0 were chosen to be representative of values near the top of the generating layer, where most of the cloud ice is assumed to be generated. Values used as input for the model are given in Table 1, along with observed ice-water mixing ratio and cloud amount.

When possible, cloud depths and their standard deviations were given by the radar cloud-boundary data. For these cases, all of the input parameters required by the model can thus be completely specified from observations, providing a stringent test of the model's utility. The aircraft sampled the three deeper cases well in the vertical (KA04, KA07 and KA14).

Observed ice-water mixing-ratio histograms are displayed in Fig. 10, with the smooth curves giving the modelled distribution, both presented as percentages so that the sum of all values for a totally overcast case is 100%. The figures are given in order of decreasing cloud amount. The distributions are reproduced extremely well considering the uncertainties in the data. The two overcast cases are predicted correctly. The model predicted 100% cloud amount for KA14. However, the cloud was in its decaying stage during the flight, resulting in a reduced cloud amount and a slightly more skewed distribution than would have been observed at an earlier stage and predicted by the model. Table 2 lists the model prediction of cloud amount and average ice-water mixing ratio and their deviations from the observed mean values.

Figure 11 shows the predicted distributions for the thin, undercast cases when larger values of σ_D are used as input, as given in Table 3. The shapes of the distributions are still well reproduced and the predicted cloud amounts and average ice-water mixing ratios are much improved. This is because the radar measures cloud depths for the existing cloud, while negative cloud depths in the model result in cloud-free regions

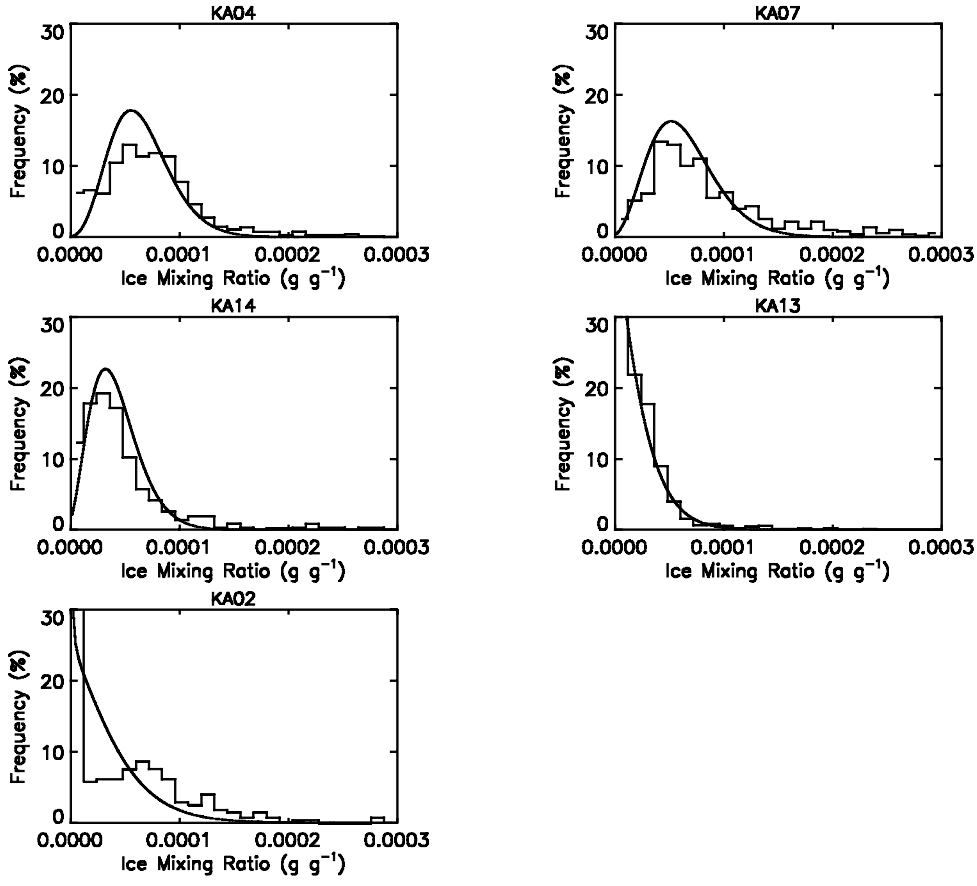

Figure 10. Histograms of ice-water mixing ratios observed during each flight for those cases with radar data available, in order of decreasing cloud amount. Smooth curves are the model-predicted ice distributions obtained using input values given in Table 1.

TABLE 2. MODEL PREDICTIONS

Flight	Radar	Predicted CA	CA error	$\overline{w_i}$	$\overline{w_i}$ error
KA04	Y	100	0%	6.5	−7%
KA07	Y	100	0%	6.3	−31%
KA14	Y	100	11%	4.2	−15%
KA13	Y	90	11%	1.9	−18%
KA02	Y	93	27%	3.2	−40%
KA07NW	N	100	0%	7.0	−24%
SA07	N	100	0%	5.9	−51%
SA05	N	89	28%	2.7	−60%
SA06	N	75	6%	1.3	−55%
SA09	N	94	34%	4.0	−65%
SA14	N	65	12%	1.9	−74%
SA13	N	58	14%	0.9	−37%
KA05	N	100	3%	4.0	124%

Model predicted cloud amount CA, model predicted average ice mixing ratio $\overline{w_i}$, and their percentage deviations from the values observed by the aircraft.

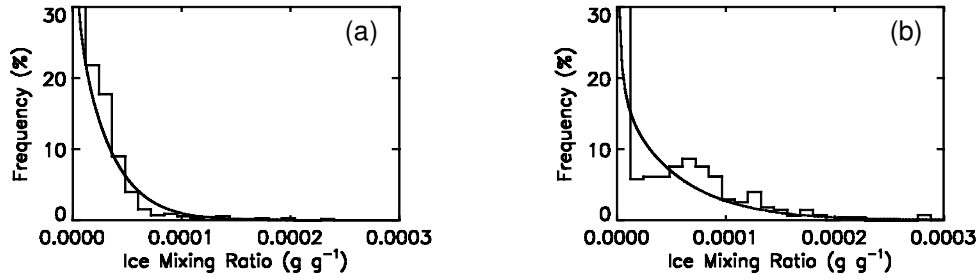

Figure 11. Model output for the cases with cloud amount $<100\%$ when the value of σ_D used as input is increased as given in Table 3. Flights (a) KA13 and (b) KA02.

TABLE 3. NEW σ_D AND RESULTING MODEL OUTPUT

Flight	New σ_D	CA	CA error	$\overline{w_i}$	$\overline{w_i}$ error
KA13	350	84	4%	2.2	−2%
KA02	450	84	15%	4.0	−25%

New values of σ_D to replace values in Table 1 for cases with CA < 100%, model-predicted cloud amount and average ice mixing ratio, and percentage deviations from the values observed by the aircraft.

which reduces the cloud fraction. Increasing σ_D accounts for this. Over all well-defined cases, the average cloud ice mixing ratio is predicted to within 31%, and cloud fraction is predicted to within 15%.

When radar data were not available, cloud depths were estimated as the distance between the lowest and highest in-cloud runs, although this may underestimate the average depth by a couple of hundred meters (more if the average cloud depth was changing in time). For these cases, σ_D is a free parameter and the only test we can perform is to choose a value which gives the observed type of distribution and ask whether the implied σ_D is plausible. Figure 12 shows the distributions predicted for these cases. The largest value of σ_D used corresponded to a turbulent case while the smallest value corresponded to the calmest case, giving some confidence that the values used are realistic.

Cloud amount was predicted to within 34% (overestimated), and the two totally overcast cases were predicted correctly. In some of these cases, a value of σ_D was found that reproduced the basic shape of the distribution. Other observed distributions had long tails towards higher ice mixing-ratio values which were not reproduced by the model, and the predicted ice-water mixing ratios were underestimated by up to 74% (see Table 2). The predicted distribution for flight SA07 was too narrow and clearly underestimated the mode value.

Some of these values of σ_D are quite large, but these correspond to cases with low cloud amounts. If the radar had observed the variation in cloud depth, a lower value of σ_D would have been obtained as described above because it is the very large negative deviations in D that create clear regions in the model. Figure 13 shows the values of σ_D/D used as input to the model plotted against the observed cloud amount. It can be seen that the same inverse relationship exists as for the radar-observed cloud-depth variability, which is encouraging.

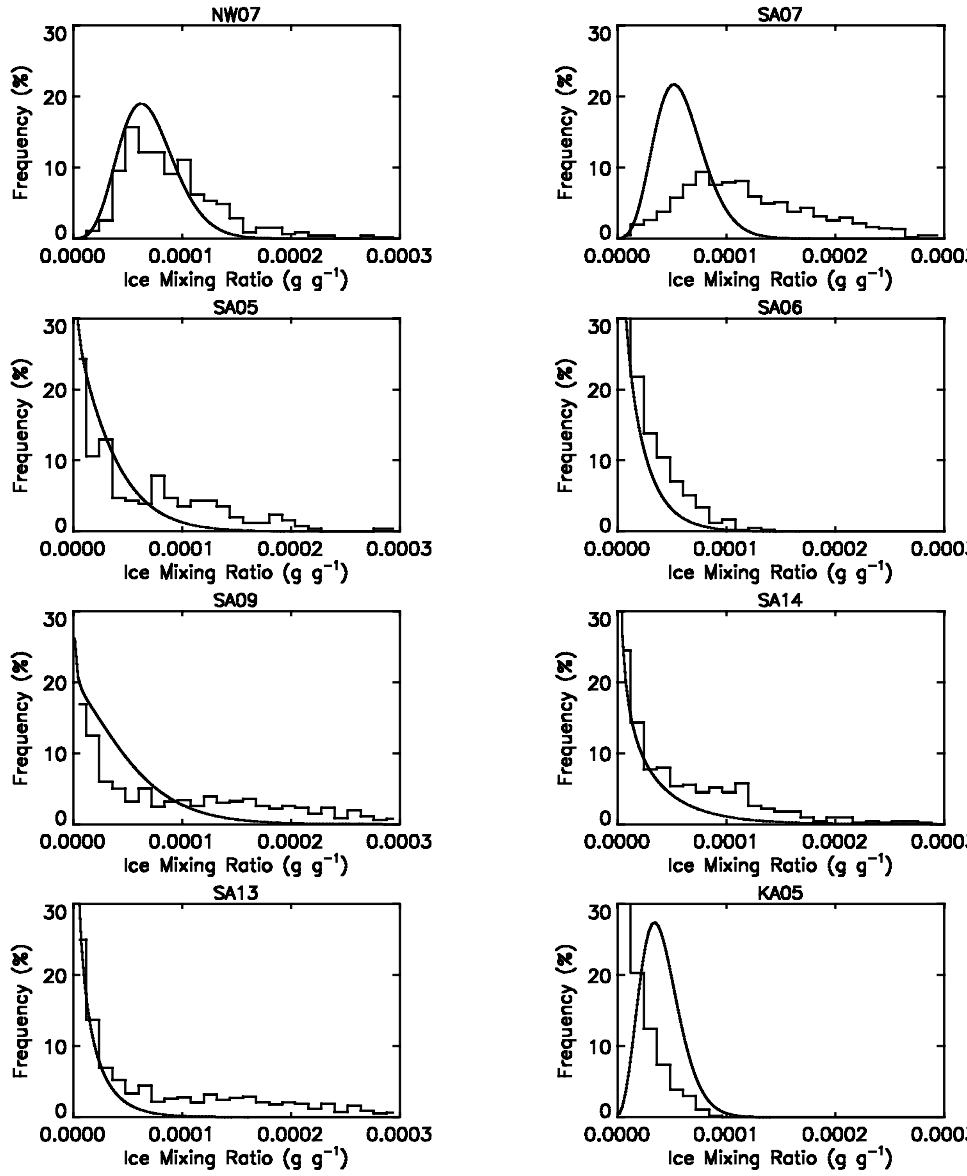

Figure 12. As in Fig. 10 but for all other cases, using input parameter values given in the lower part of Table 1.

An attempt to improve the agreement with observations for these cases was made by changing the values of A_0 and D_G. Doubling the value of A_0 improves the ice distributions (particularly for case SA07), improves the predicted cloud fraction by up to 8% and improves the predicted average ice mixing ratio by between 45% and 10%. This indicates that the discrepancies between the model and the observations may be attributed to errors in the estimation of A_0 and D_G, which are difficult to calculate accurately given the low resolution of the aircraft data. They may also be due to the shifting of the generating layer to lower levels where A_0 tends to be larger, as the cirrus cloud develops and grows downwards owing to ice-crystal fallout. Differences in the

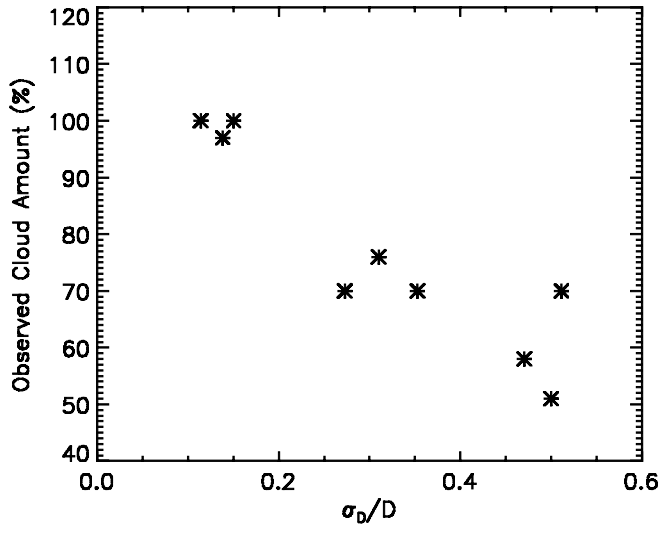

Figure 13. Observed cloud amount against normalized variations of cloud depth D chosen as model input for cases without radar data available.

distributions may also result from incomplete sampling of the cirrus by the aircraft and because of changes in time.

The model produces a distribution for KA05 which has the wrong shape (Fig. 12). This case was previously seen to be an exception to the general behaviour of the ice-content distribution, peaking at the lowest value and decreasing monotonically despite having a high cloud fraction. The model gives the correct cloud amount (basically overcast, Table 2), but overestimates the average ice mixing ratio by 124%. The modelled pdf is almost Gaussian. Halving the D_G to 500 m produces a distribution similar to that observed with average ice mixing ratio 35% smaller than observed and the correct cloud amount. It is hard to say which are the correct input values. It is possible that the aircraft overestimated the cloud amount by flying deliberately into cloud. If this was the case, however, we might expect to see evidence of this for other flights. On the other hand, the value of D_G necessary to produce a similar distribution, assuming the aircraft-observed cloud amount is correct, appears to be too small compared to the observed regions of saturation. High shear and stability were observed by radiosonde ascents through the cloud layer. This may have caused individual generating layers to remain thin, with no interaction between them. There was very little turbulence or convection in this case, with mostly wave-like motions. An alternative explanation for the failure of the model in this case is that the wind shear may have transported ice into otherwise clear regions, reducing the average ice mixing ratio within the cloud and increasing the cloud amount. If this is the case, the above model will not work because the effect of shear on the ice distribution is not accounted for. Vertical wind shear will seriously affect the model when the distance moved by the cirrus top relative to the base is a significant fraction of the cloud dimension. During flight KA05 there was a shear of 1.1×10^{-2} s^{-1} over a total cloud depth of 2 km. Over 1 hour the top would have been advected 80 km further than the base, which is comparable to the size of the cloud itself. The environment was also stable so that convection and vertical mixing were inhibited.

7. Conclusions

The ice-water mixing-ratio histograms obtained from horizontal runs during the FIRE-II cirrus flights are found to be almost Gaussian when cloud amount is 100% and have obvious modal values. The histogram shape changes at lower cloud amounts to one which peaks at the lowest measured value and decreases monotonically. The ISCCP derived optical-depth histograms behave in a similar fashion.

A simple model of cirrus horizontal inhomogeneity has been formulated which assumes a Gaussian distribution of cloud depth and that all internal horizontal inhomogeneity in the ice mixing ratio is due to variations in the cloud depth. Ice is assumed to form originally in a cloud-top generating region (defined as the supersaturated region) with the IWP related to D_G. The effect of ice sedimentation on the ice-water mixing ratio is included by dividing IWP by the entire depth of the cloud for comparison with aircraft ice-water content distributions. This requires the simplifying assumption that the average ice-water mixing ratio is independent of height in the cloud, justified by the variation in the observed ice profiles. The use of such a model is suggested by the observed relationship between the normalized variability of cloud depth and both the normalized variability of the ice-water mixing ratio (and extinction) and the cloud amount.

The observed ice mixing-ratio distributions are reproduced well by the model for well-defined cases (those which were well sampled by the aircraft in the vertical and had radar observations of cloud boundary statistics available) using best estimates of D_G and A_0, although these two parameters cannot be determined very accurately. Cloud amount was predicted to within 15% of the observed value. The average ice mixing ratio was predicted with varying success, but to within 31% for the cases with observed σ_D. For most of the other cases, a plausible value of σ_D can be found which produces a realistic ice distribution. These values of σ_D/D had the same relationship with observed cloud fraction as those observed by the radar. It seems that any discrepancies between the modelled and observed ice distributions can be attributed to errors in the estimation of A_0 or D_G, which are quite difficult to obtain accurately, especially considering the low vertical resolution of the aircraft observations. The main weakness in the model is its inability to account for the effect of very high shear on the ice distributions, as in the case of KA05.

This conceptual model could be used as a starting point for the development of a GCM parametrization of the ice mixing-ratio pdf and a more physically based estimate of cloud amount. To do so would require the specification of the model input parameters A_0, D_G and σ_D from the parameters resolved by the GCM; A_0 can be calculated directly from the values of temperature and humidity at the base of a layer in which the GCM's prognostic cloud water parametrization predicts ice formation; D_G, which is comparable to or less than the thickness of typical GCM upper-troposphere layers, might be estimated by lifting a parcel with layer-mean temperature and humidity values from the layer base to its LCL and then to the layer top, defining a generating-layer base and top. The top might be estimated instead by lifting at a rate given by the grid-scale vertical velocity (Heymsfield and Donner 1990) or a prescribed mesoscale velocity in the presence of diagnosed gravity waves or convection (Donner 1993). Each of these methods would give the layer-mean IWC as well. Alternatively, if the GCM predicts IWC in some other way, regressions such as those in Fig. 6, combined with the fact that D is larger than D_G by a factor of 2 to 3 on average (Table 1), could be used to estimate D_G.

Given the pdf of IWC, one then needs to predict radiative properties and microphysical process rates. The similarity between the shapes of our IWC histograms and nearly coincident ISCCP optical-thickness histograms (Figs. 4 and 5) argues that IWC

captures much of the variability of radiative properties. Heymsfield and McFarquhar (1996) show that cross-sectional area (and thus extinction) measurements of tropical cirrus fit well a relation of the form $\beta = C(\mathrm{IWC})^n$, where C is a constant and $n \sim 0.9$ over a wide range of temperatures. Since $n = 1$ implies that r_e is independent of IWC, it appears that particle size increases only slightly but systematically as a function of IWC, so that knowledge of IWC alone is sufficient to predict much of the variation in cloud extinction. In our FIRE-II dataset for midlatitude cirrus, we find a similar relationship but with $n \sim 1$, which is not significantly different from the Heymsfield and McFarquhar result given the small number of FIRE-II points in our sample. Figure 5 shows that D also increases systematically with IWC, so $\tau = \beta \times D$ should be a function of IWC as well; we find that $\tau \propto (\mathrm{IWC})^{1.7}$ provides a fairly good fit to the FIRE-II data. Heymsfield (1977) shows that ice fallout speeds vary approximately as $(\mathrm{IWC})^{0.16}$. Pincus and Klein (2000) show how process rates that are nonlinear functions of cloud water content can be generalized from the cloud scale to the GCM grid scale given knowledge of the cloud water pdf. Such an approach, in which everything required by the GCM is related to the IWC pdf, is not only consistent with the available data but seems preferable at this time to a more complex strategy requiring joint pdfs of IWC, r_e and N, where N is the ice-crystal number concentration, especially given the difficulty in measuring crystal number concentration and our inadequate knowledge of both ice-nuclei distributions and the parameters controlling ice nucleation.

The parametrization problem then reduces to the question of how to determine σ_D. Plausibly this might be related to GCM parametrized turbulence levels or indirectly to the simulated static stability, wind shear or Richardson number. Whether this accounts for the observed variation of σ_D/D in Fig. 6 is not clear from the small number of cases we have to analyse, although Smith and Del Genio (2001) do find a strong negative correlation between σ_D/D and mean static stability over the cloud depth. What is needed is a climatology of cirrus cloud depths and their variability under different meteorological conditions. Such a dataset is being compiled by the Millimeter Cloud Radar deployed by the Atmospheric Radiation Measurement program in the Southern Great Plains, USA. It is important to note that GCM parametrizations are inherently statistical in nature, since they do not have information about instantaneous small-scale forcing, and hence they cannot predict instantaneous subgrid distributions, nor do they have to for climate purposes. The scatter in Fig. 6, and the failure of the conceptual model for flight KA05, demonstrate that the horizontal ice distribution will be estimated well in some cases and not as well in others. Long-term cloud radar climatologies will help determine whether such difficult cases are more the exception or the rule and thus whether a parametrization based on the conceptual model described here is feasible. We anticipate that the model should apply to any highly turbulent cirrus regime where small-scale vertical motions dominate the variability, including frontal, jet streak and convective blow-off situations. On the other hand, thin tropopause cirrus, which form in a very stable environment and might not be thick enough to radiatively generate turbulence, might not be well portrayed by the model presented here. Likewise, the KA05 example suggests that the model might have to be modified for high wind-shear situations. One possible effect of shear might be to decouple the upper portion of the cloud by advecting it horizontally relative to the lower portion. In such a case the cloud areal extent might be greater, but the mean depth less, for a given amount of ice formation. The fact that we had to halve D_G to get a good model fit to this case tentatively supports such an interpretation. For this to be a factor, the integral of the shear over the cloud depth and GCM physics time step would have to be a significant fraction of the cloud horizontal dimension. It is also important to observe cloud types other

than cirrus and the marine stratocumulus analysed by Considine *et al.* (1997) to know whether the behaviour they and we see is universal. However, any GCM representation of cloud water pdfs is likely to improve upon the radiation and microphysics process biases caused by the delta function pdfs now used by GCMs.

ACKNOWLEDGEMENTS

This work was supported by the NASA FIRE-II Research Program and the DOE Atmospheric Radiation Measurement Program. Microphysical data were provided by Andrew Heymsfield.

REFERENCES

Cahalan, R. F., Ridgway, W., Wiscombe, W. J., Bell, T. L. and Snider, J. B. 1994 The albedo of fractal stratocumulus cloud. *J. Atmos. Sci.*, **51,** 2434–2455

Considine, G., Curry, J. A. and Wielicki, B. 1997 Modeling cloud fraction and horizontal variability in marine boundary layer clouds. *J. Geophys. Res.*, **102,** 13517–13525

Del Genio, A. D., Yao, M.-S., Kovari, W. and Lo, K. K.-W. 1996 A prognostic cloud water parameterization for global climate models. *J. Climate*, **9,** 270–304

Donner, L. J. 1993 A cumulus parameterization including mass fluxes, vertical momentum dynamics, and mesoscale effects. *J. Atmos. Sci.*, **50,** 889–906

Donner, L. J., Seman, C. J., Soden, B. J., Hemler, R. S., Warren, J. C., Strom, J. and Liou, K.-N. 1997 Large-scale ice clouds in the GFDL SKYHI GCM. *J. Geophys. Res.*, **102,** 21745–21768

Foot, J. S. 1988 Some observations of the optical properties of clouds. II: Cirrus. *Q. J. R. Meteorol. Soc.*, **114,** 145–164

Fu, Q. 1996 An accurate parametrization of the solar radiative properties of cirrus clouds for climate models. *J. Climate*, **9,** 2058–2082

Heymsfield, A. J. 1977 Precipitation development in stratiform ice clouds: A microphysical study. *J. Atmos. Sci.*, **34,** 367–381

Heymsfield, A. J. and Baumgardner, D. 1985 Summary of a workshop on processing 2D probe data. *Bull. Am. Meteorol. Soc.*, **66,** 437–440

Heymsfield, A. J. and Donner, L. J. 1990 A scheme for parameterizing ice-cloud water content in general circulation models. *J. Atmos. Sci.*, **47,** 1865–1877

Heymsfield, A. J. and McFarquhar, G. M. 1996 High albedos of cirrus in the tropical Pacific warm pool: Microphysical interpretations from CEPEX and from Kwajalein, Marshall Islands. *J. Atmos. Sci.*, **53,** 2424–2451

Heymsfield, A. J. and Milosevich, L. 1995 Relative humidity and temperature influences on cirrus formation and evolution: Observations from wave clouds and FIRE-II. *J. Atmos. Sci.*, **52,** 4302–4326

Heymsfield, A. J., Miller, K. M. and Spinhirne, J. D. 1990 27–28 October FIRE case: Cloud microphysics. *Mon. Weather Rev.*, **118,** 2313–2328

Knollenberg, R. G. 1970 The optical array: An alternative to scattering or extinction for airborne particle size determination. *J. Appl. Meteorol.*, **9,** 86–103

Liou, K. N. and Rao, N. 1996 Radiative transfer in cirrus clouds. Part 4: On cloud geometry, inhomogeneity, and absorption. *J. Atmos. Sci.*, **53,** 3046–3065

Mace, G. G., Ackerman, T. P., Clothiaux, E. E. and Albrecht, B. B. 1997 A study of composite cirrus morphology using data from a 94 GHz radar and correlations with temperature and large-scale vertical motion. *J. Geophys. Res.*, **102,** 13581–13593

Pincus, R. and Klein, S. A. 2000 Unresolved spatial variability and microphysical process rates in large-scale models. *J. Geophys. Res.*, **105**, 27059–27065

Rossow, W. B. and Schiffer, R. A. 1991 ISCCP cloud data products. *Bull. Am. Meteorol. Soc.*, **72,** 2–20

Smith, S. A. and Del Genio, A. D. 2001 Analysis of aircraft, radiosonde and radar observations in cirrus clouds observed during FIRE-II: The interactions between environmental structure, turbulence and cloud microphysical properties. *J. Atmos. Sci.*, **58,** 451–461

Tsay, S., Gabriel, P. M., King, M. D. and Stephens, G. L. 1996 Spectral reflectance and atmospheric energetics in cirrus-like clouds. Part 2: Applications of a Fourier–Riccati approach to radiative transfer. *J. Atmos. Sci.*, **53,** 3450–3467

Uttal, T., Clothiaux, E. E., Ackerman, T. P., Intrieri, J. M. and Eberhard, W. L. 1995 Cloud boundary statistics during FIRE-II. *J. Atmos. Sci.*, **52,** 4276–4284

Wielicki, B. A. and Parker, L. 1994 'Frequency distribution of cloud liquid water path in oceanic boundary layer cloud as a function of cloud fraction'. Pp. 415–417 in Preprints of 8th AMS conference on atmospheric radiation, 23–28 January 1994, Nashville, TN, USA. American Meteorological Society, Boston